SUPPLEMENTARY INFORMATION

Dry and warm conditions in Australia exacerbated by aerosol reduction in China

Jiyuan Gao[1], Yang Yang[1*], Hailong Wang[2], Pinya Wang[1], Hong Liao[1]

[1]Joint International Research Laboratory of Climate and Environment Change (ILCEC), Jiangsu Key Laboratory of Atmospheric Environment Monitoring and Pollution Control, Jiangsu Collaborative Innovation Center of Atmospheric Environment and Equipment Technology, School of Environmental Science and Engineering, Nanjing University of Information Science and Technology, Nanjing, Jiangsu, China

[2]Atmospheric, Climate, and Earth Sciences Division, Pacific Northwest National Laboratory, Richland, Washington, USA

*Correspondence to yang.yang@nuist.edu.cn

Contents of this file

Table S1: Experimental design.

Experiments	Anthropogenic Emissions of Aerosols and Precursors	
	China	Other regions of the world
BASE	2013	2013
CHN	2019	2013
OTH	2013	2019
NAEU	2013	North America and Europe: 2019; Other: 2013

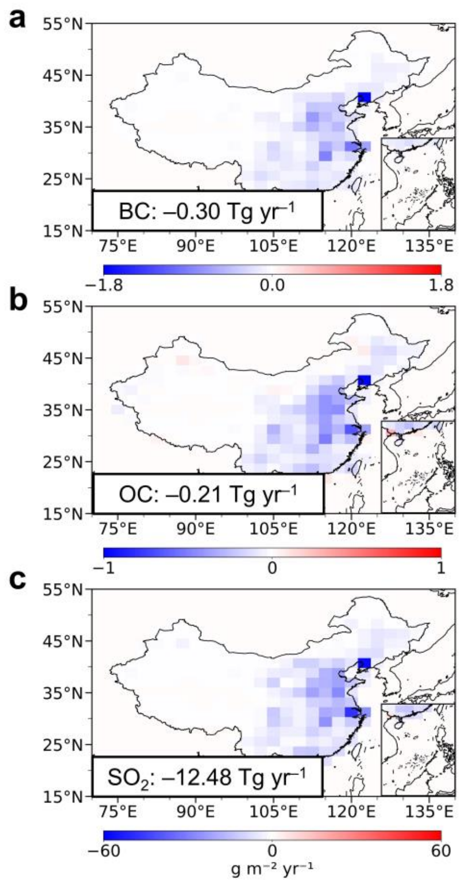

Figure S1. Differences in anthropogenic emissions of aerosols and precursors between 2013 and 2019. Spatial distributions of differences in anthropogenic emissions (unit: g m^{-2} yr^{-1}) of aerosols and precursors, including black carbon (BC, **a**), organic carbon (OC, **b**) and sulfur dioxide (SO_2, **c**) between 2013 and 2019 (2019 minus 2013). The total changes in China are noted at the bottom-left corner of each panel.

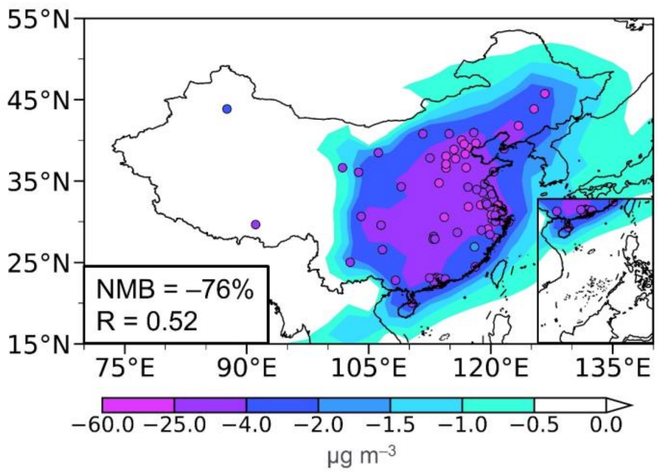

Figure S2. Comparisons of temporal changes in near-surface $PM_{2.5}$ concentrations between observation and model simulation. Spatial distributions of observed (circles) and modeled (shades) annual mean changes (2017–2019 minus 2013–2015) in near-surface $PM_{2.5}$ concentration (unit: μg m^{-3}). Normalized mean bias (NMB) and correlation coefficient (R) between observation and simulation are shown at the bottom-left corner of each panel. $NMB = 100\ \% \times \sum (Model_i - Observation_i) / \sum Observation_i$, where $Model_i$ and $Observation_i$ are the modeled and observed values at site i, respectively.

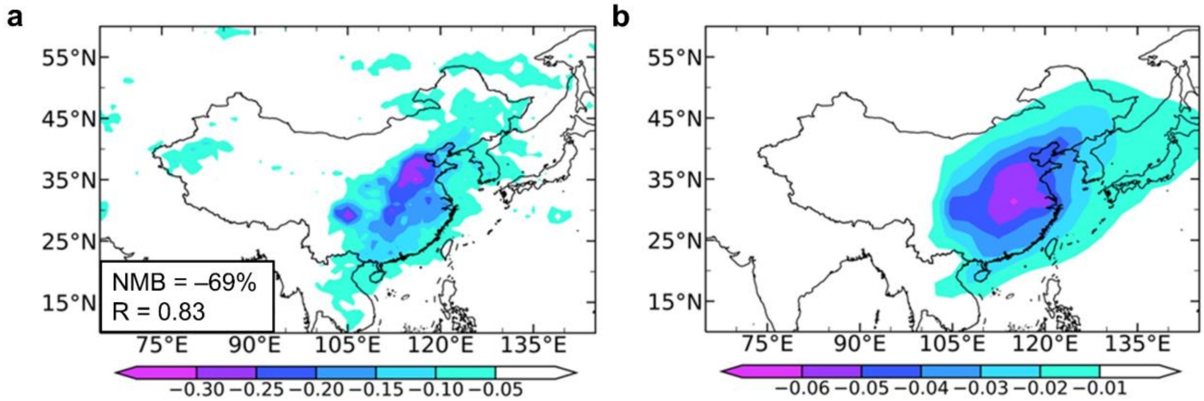

Figure S3. Comparisons of temporal changes in aerosol optical depth (AOD) between satellite retrieval and model simulation. Spatial distributions of annual mean changes (2017–2019 minus 2013–2015) in Moderate Resolution Imaging Spectroradiometer (MODIS) (**a**) and modeled (**b**) AOD (unitless). Normalized mean bias (NMB) and correlation coefficient (R) between modeled AOD and MODIS AOD are shown at the bottom-left corner of panel a. $NMB = 100\,\% \times \sum (AOD\text{-}model_i - AOD\text{-}MODIS_i) / \sum AOD\text{-}MODIS_i$, where $AOD\text{-}model_i$ and $AOD\text{-}MODIS_i$ are the modeled and MODIS AOD values at grid i, respectively.

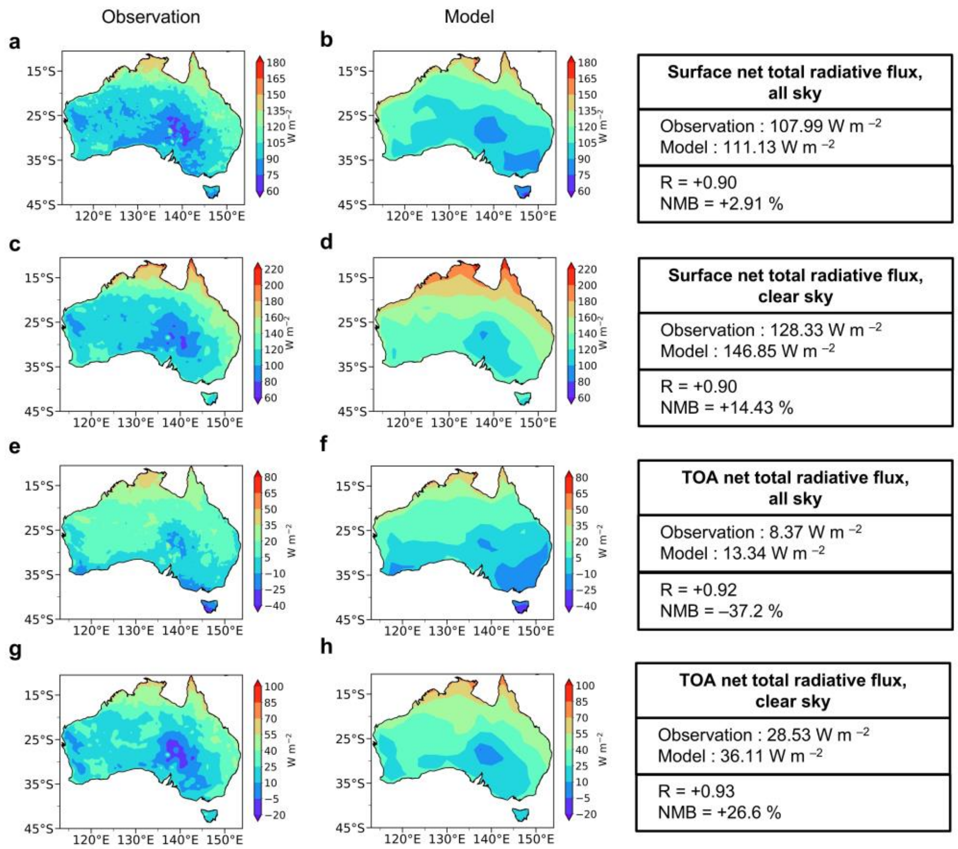

Figure S4. Comparisons of surface and TOA net total radiative flux under all sky and clear sky conditions between observation and model simulation. Spatial distributions of surface (**a**–**d**) and TOA (**e**–**h**) net total radiative flux (unit: W m^{-2}) under all sky (**a**, **b**, **e**, and **f**) and clear sky (**c**, **d**, **g**, and **h**) conditions over Australia in observation (2010–2019 annual averages from ERA5, **a**, **c**, **e**, and **g**) and model simulation (annual averages from the BASE experiment, **b**, **d**, **f**, and **h**). Regional averages over Australia in observation and model simulation and normalized mean bias (NMB) and correlation coefficient (R) between observation and model simulation are shown in the right boxes.

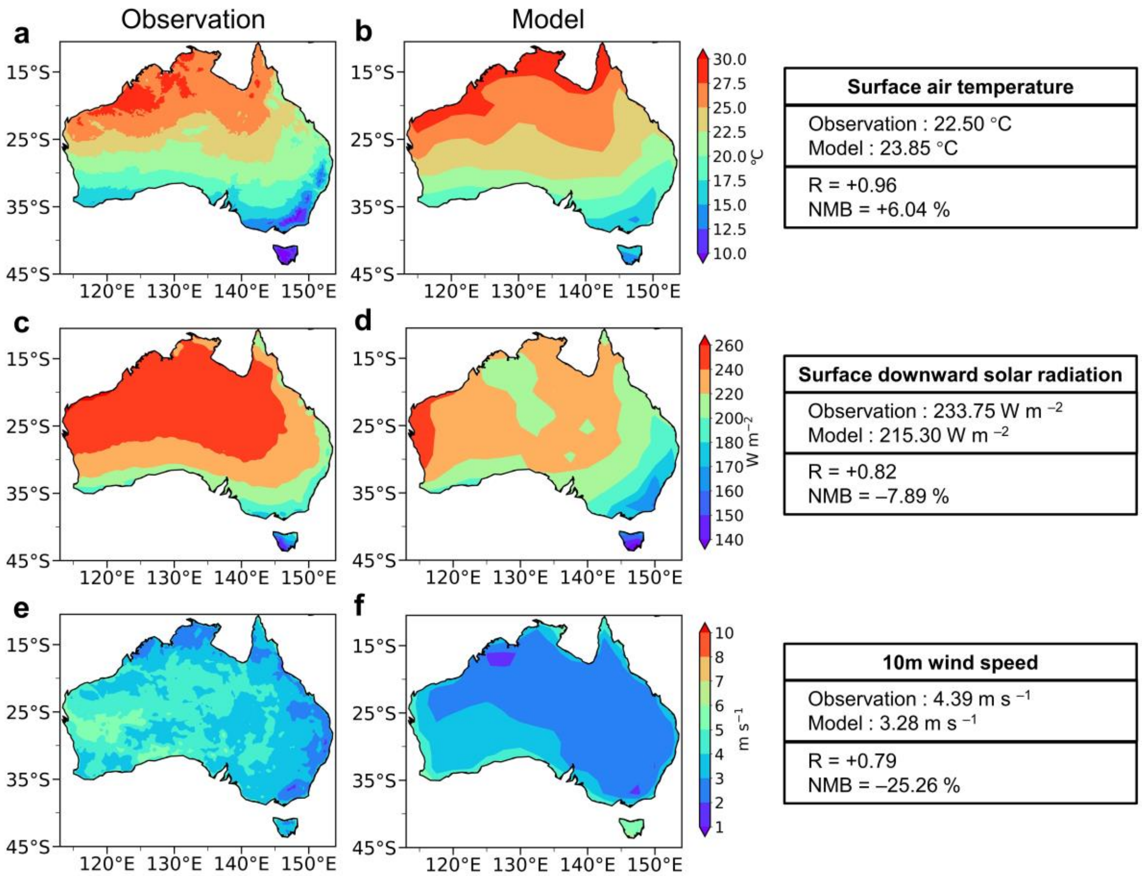

Figure S5. Comparisons of surface air temperature, surface downward solar radiation, and 10m wind speed between observation and model simulation. Same as Figure S4, but for surface air temperature (**a** and **b**, unit: °C), surface downward solar radiation (**c** and **d**, unit: W m^{-2}) and 10m wind speed (**e** and **f**, unit: m s^{-1}).

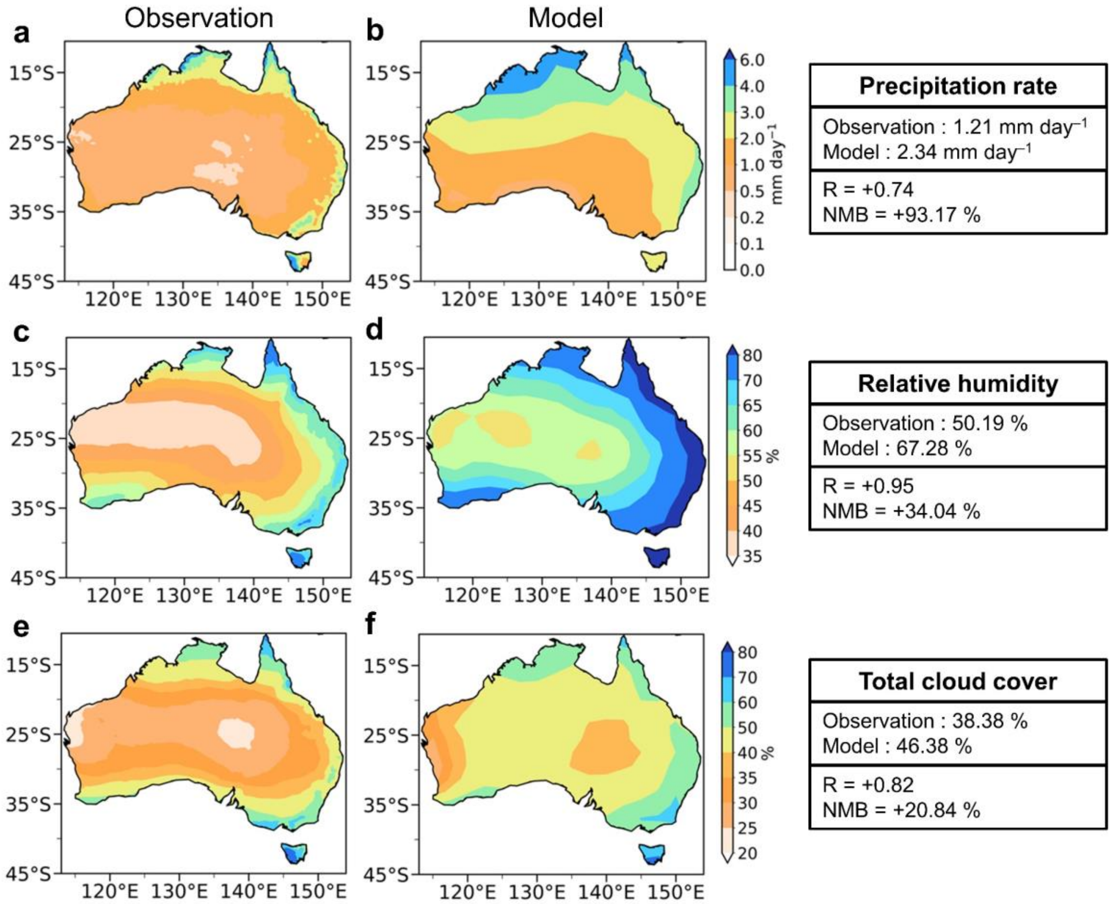

Figure S6. Comparisons of precipitation rate, relative humidity and total cloud cover between observation and model simulation. Same as Figure S4, but for precipitation rate (**a** and **b**, unit: mm day^{-1}), relative humidity (**c** and **d**, unit: %), and total cloud cover (**e** and **f**, unit: %).

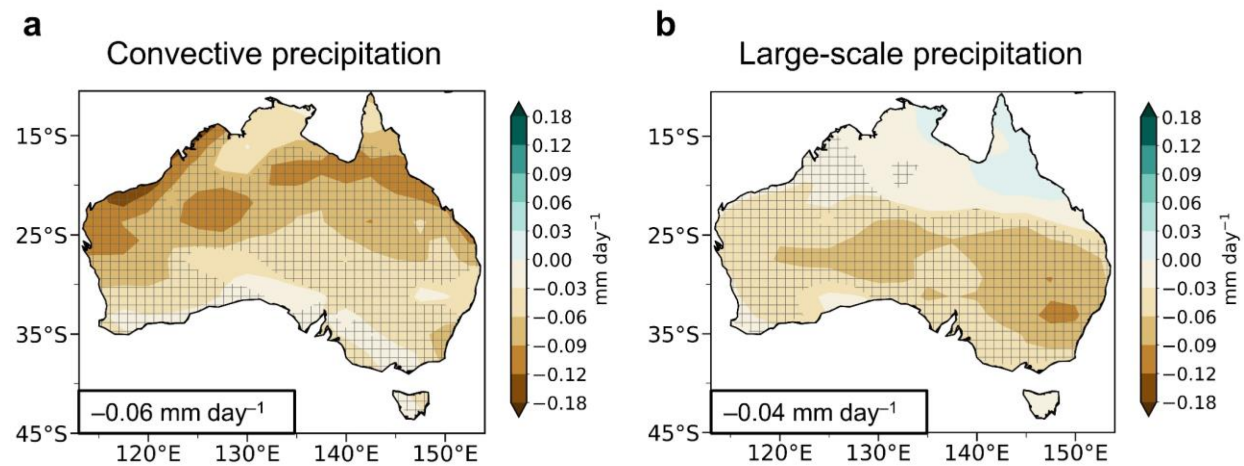

Figure S7. Simulated changes in convective and large-scale precipitation rate in Australia due to aerosol changes in China between 2013 and 2019. Spatial distributions of simulated differences in annual mean convective (**a**) and large-scale (**b**) precipitation rate (unit: mm day^{-1}) in Australia between BASE and CHN (CHN minus BASE). The shaded areas indicate results are statistically significant at the 90% confidence level. Regional averages of the responses over Australia are noted at the bottom-left corner of each panel.

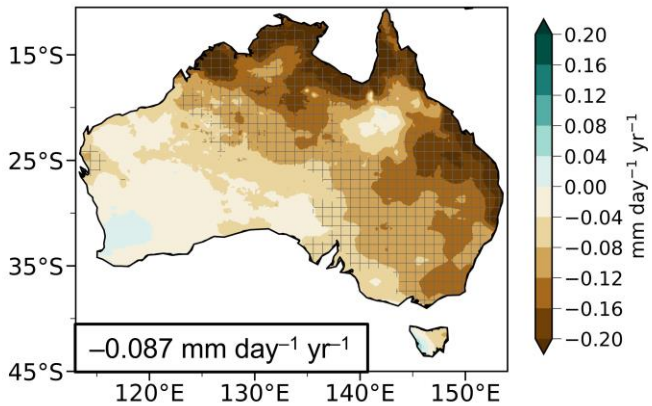

Figure S8. Linear trends of observed precipitation rate in Australia based on GPM. Spatial distributions of linear trends of annual mean precipitation rate (unit: mm day^{-1} yr^{-1}) in Australia during 2010–2019 from GPM. The shaded areas indicate trends are statistically significant at the 90% confidence level. Regional averages over Australia are noted at the bottom-left corner of the panel.

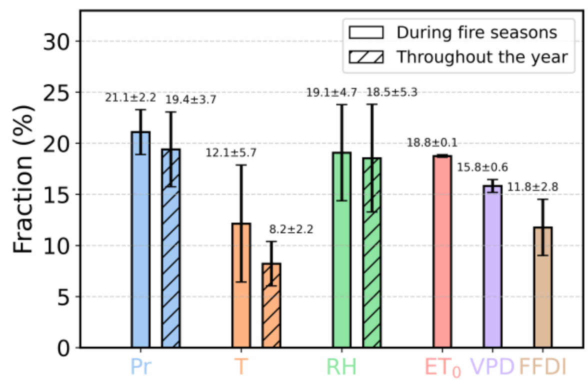

Figure S9. Fractional contributions of the observed changes in climate variables and wildfire risk indices attributable to aerosol changes in China. Fractional contributions (unit: %) of the observed changes in climate variables (precipitation rate [Pr], surface air temperature [T], and relative humidity [RH]) during fire seasons and throughout the year and wildfire risk indices (reference potential evapotranspiration [ET_0], vapor pressure deficit [VPD], and McArthur forest fire danger index [FFDI]) during fire seasons attributable to aerosol changes in China. Error bar represents the standard deviation of 3-ensemble members.

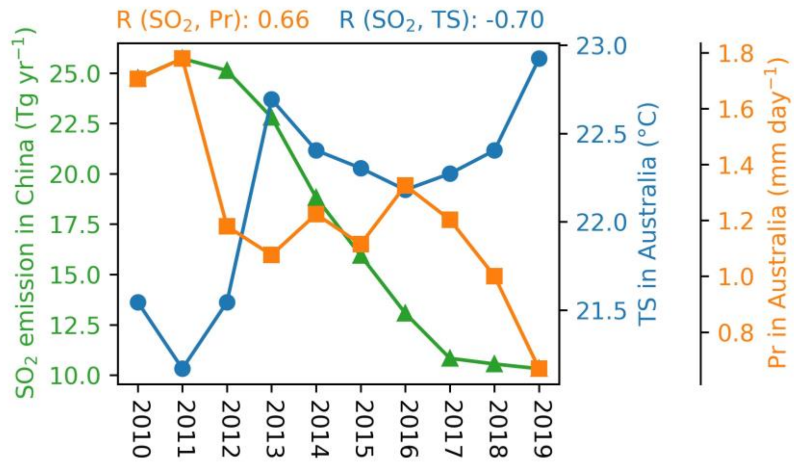

Figure S10. Time series of anthropogenic SO_2 emission in China alongside surface air temperature and precipitation rate averaged over Australia. SO_2 emission (unit: Tg yr^{-1}) data are sourced from CEDS, while surface air temperature (unit: °C) and precipitation rate (unit: mm day^{-1}) data are derived from ERA5. Correlations between SO_2 emission in China and surface air temperature averaged over Australia, as well as between SO_2 emission in China and precipitation rate averaged over Australia, are indicated above the figure.

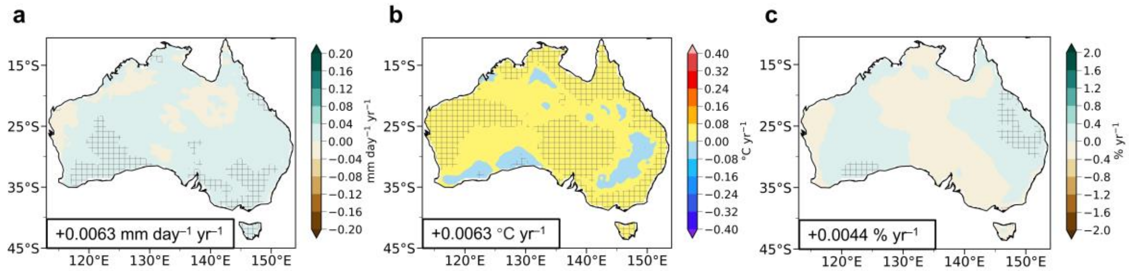

Figure S11. Linear trends of observed precipitation rate, surface air temperature and relative humidity in Australia during 1940–2019 based on ERA5. Spatial distributions of linear trends of annual mean precipitation rate (**a**, unit: mm day^{-1} yr^{-1}), surface air temperature (**b**, unit: °C yr^{-1}) and relative humidity (**c**, unit: % yr^{-1}) in Australia during 1940–2019 from ERA5. The shaded areas indicate trends are statistically significant at the 90% confidence level. Regional averages over Australia are noted at the bottom-left corner of each panel.

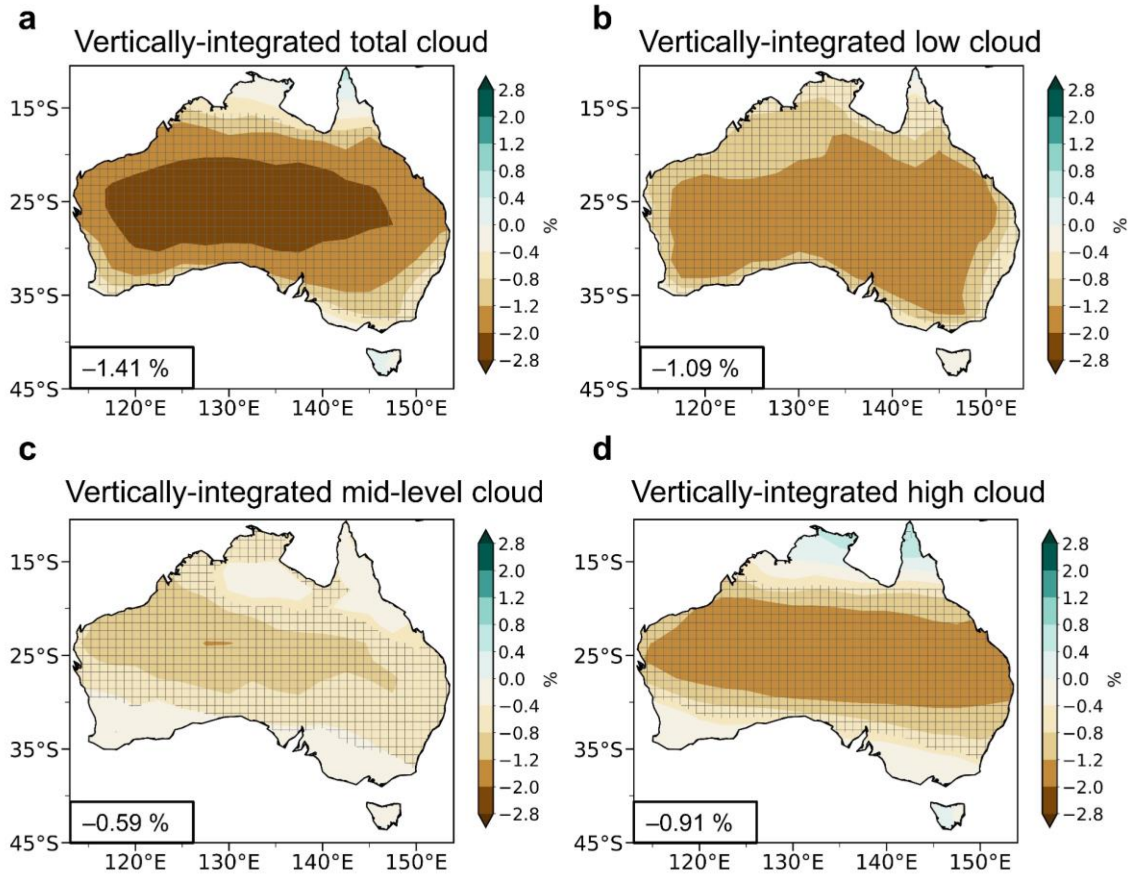

Figure S12. Changes in vertically-integrated total, low, mid-level, and high cloud cover in Australia due to aerosol changes in China between 2013 and 2019. Spatial distributions of simulated differences in annual mean vertically-integrated total (**a**), low (**b**), mid-level (**c**), and high (**d**) cloud cover (unit: %) in Australia between BASE and CHN (CHN minus BASE). The shaded areas indicate results are statistically significant at the 90% confidence level. Regional averages of the responses over Australia are noted at the bottom-left corner of each panel.

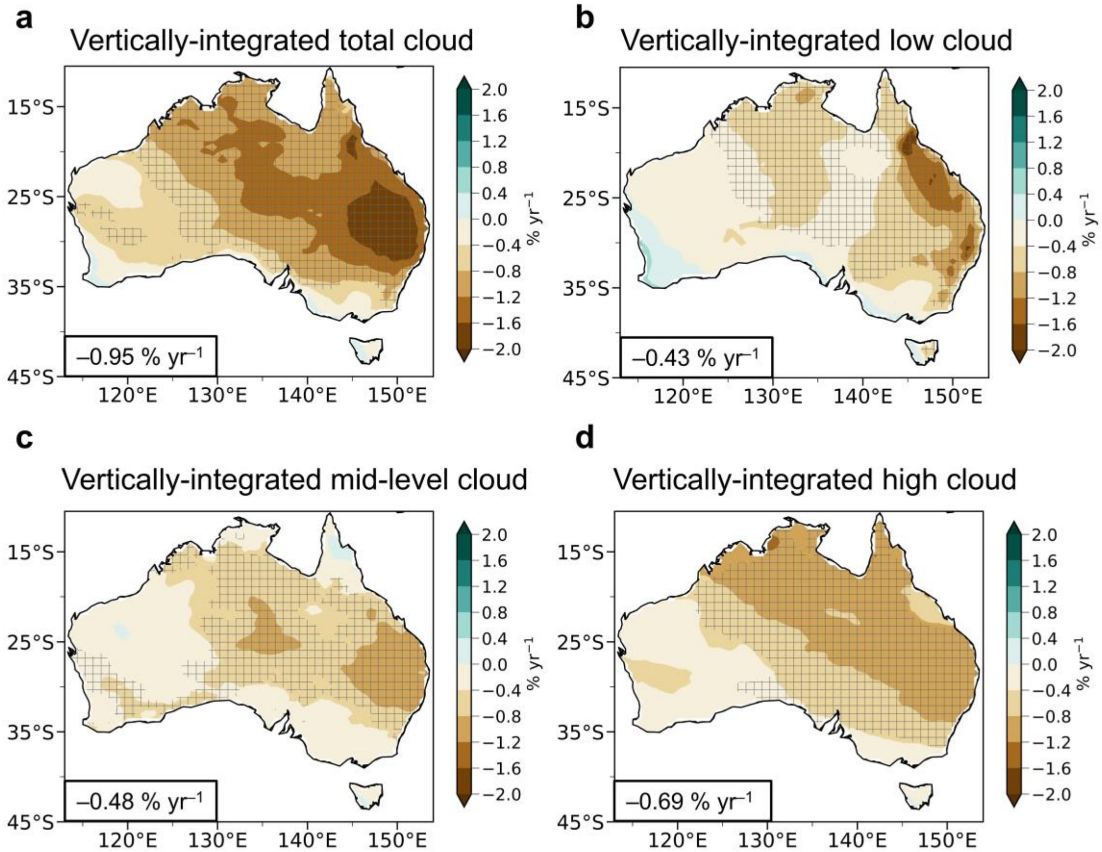

Figure S13. Linear trends of observed vertically-integrated total, low, mid-level, and high cloud cover in Australia based on ERA5. Spatial distributions of linear trends in annual mean vertically-integrated total (**a**), low (**b**), mid-level (**c**), and high (**d**) cloud cover (unit: % yr^{-1}) in Australia during 2010–2019 from ERA5. The shaded areas indicate trends are statistically significant at the 90% confidence level. Regional averages over Australia are noted at the bottom-left corner of each panel.

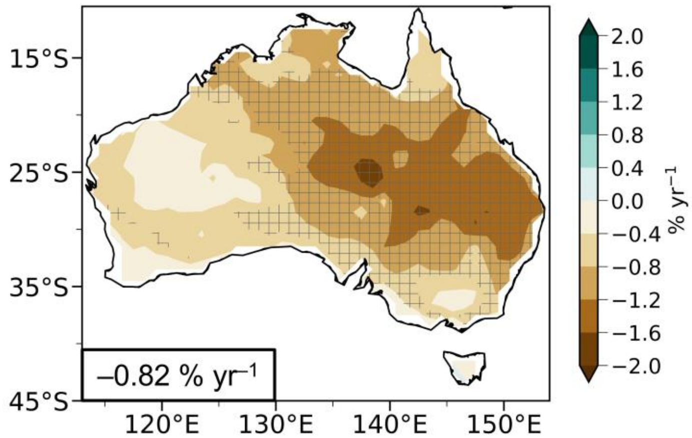

Figure S14. Linear trends of observed total cloud cover in Australia based on CERES-EBAF. Spatial distributions of linear trends of annual mean vertically-integrated total cloud cover (unit: % yr^{-1}) in Australia during 2010–2019 from CERES-EBAF. The shaded areas indicate trends are statistically significant at the 90% confidence level. Regional averages over Australia are noted at the bottom-left corner of the figure.

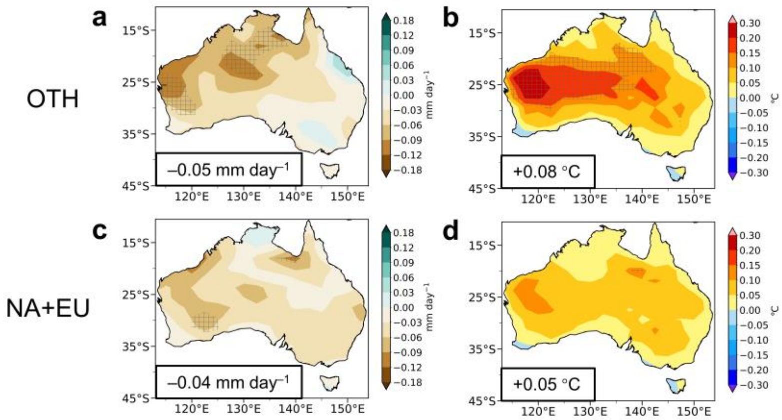

Figure S15. Simulated changes in precipitation rate and surface air temperature in Australia due to aerosol changes in different regions between 2013 and 2019. Spatial distributions of simulated differences in annual mean precipitation rate (**a** and **c**, unit: mm day^{-1}) and surface air temperature (**b** and **d**, unit: °C) in Australia between BASE and OTH (OTH minus BASE, **a** and **b**), and between BASE and NAEU (NAEU minus BASE, **c** and **d**). The shaded areas indicate results are statistically significant at the 90% confidence level. The regional averages over Australia is noted at the bottom-left corner of each panel.

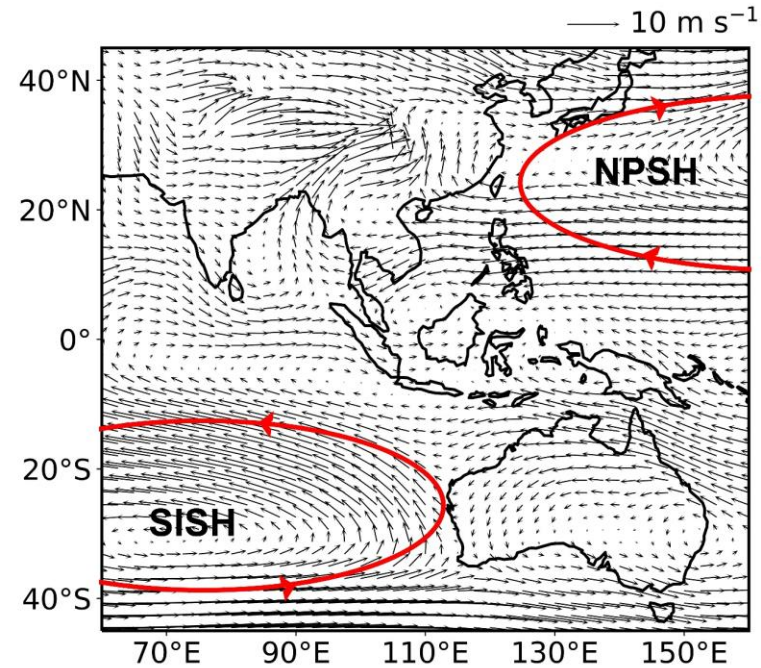

Figure S16. Climatological mean wind fields at 850 hPa. Climatological mean wind fields (unit: m s^{-1}, vectors) at 850 hPa from the BASE experiment. NPSH and SISH shown in red circles represents North Pacific Subtropical High and Southern Indian ocean Subtropical High, respectively.

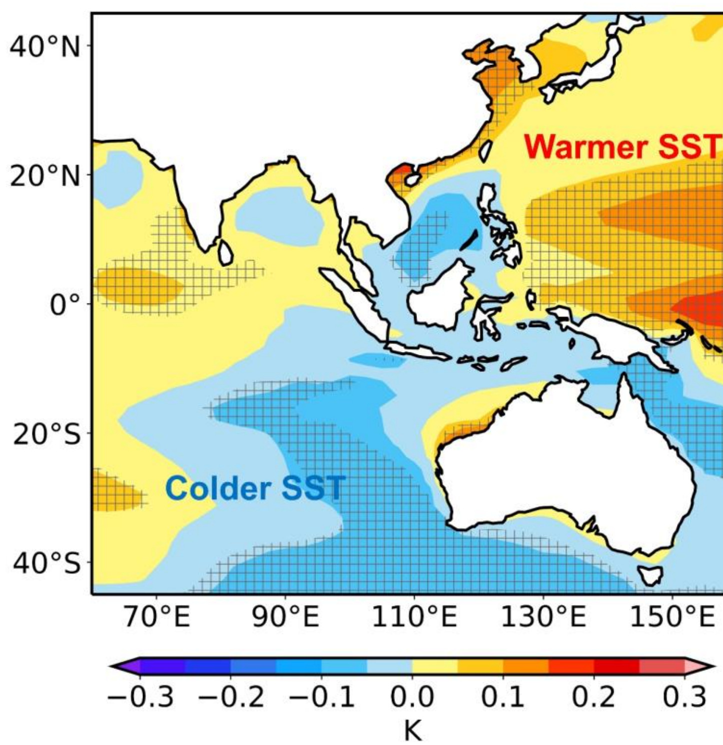

Figure S17. Simulated sea surface temperature changes due to aerosol changes in China between 2013 and 2019. Spatial distributions of simulated differences in annual mean sea surface temperature (SST, unit: mm day^{-1}) in Australia between BASE and CHN (CHN minus BASE). The shaded areas indicate results are statistically significant at the 90% confidence level.

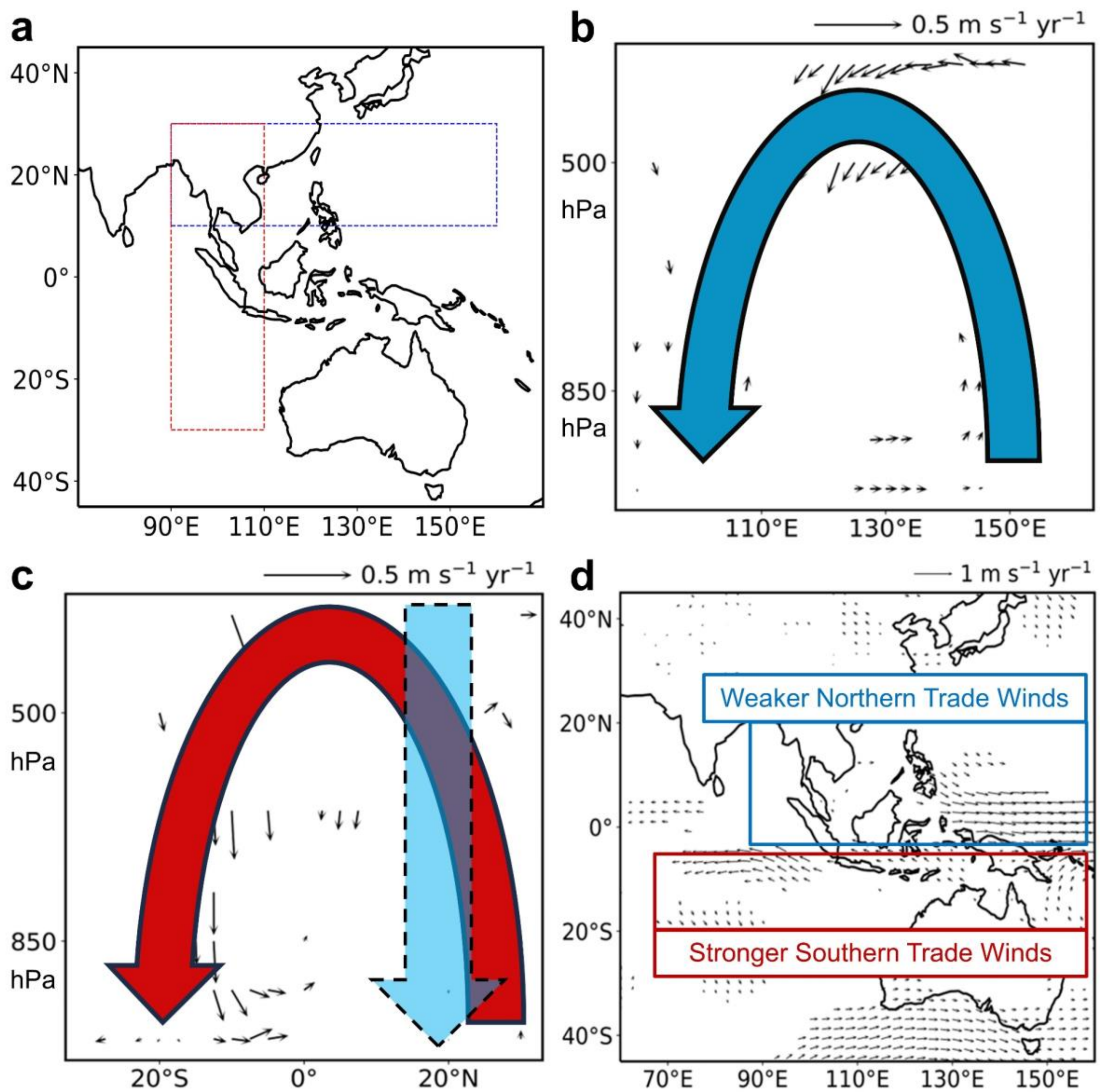

Figure S18. Linear trends in observed vertical circulations and 850 hPa wind fields in Asia-Pacific regions. Panel **b** and **c** shows pressure–longitude and latitude cross-section of linear trends in annual mean atmospheric circulations (unit: m s^{-1}, vectors) over areas marked with the blue and red box in panel **a** during 2010–2019 from ERA5. Panel **d** shows linear trends of wind fields (unit: m s^{-1}, vectors) at 850 hPa in Asia-Pacific regions. Only trends of atmospheric circulations and winds which are statistically significant at the 90% confidence level are shown.

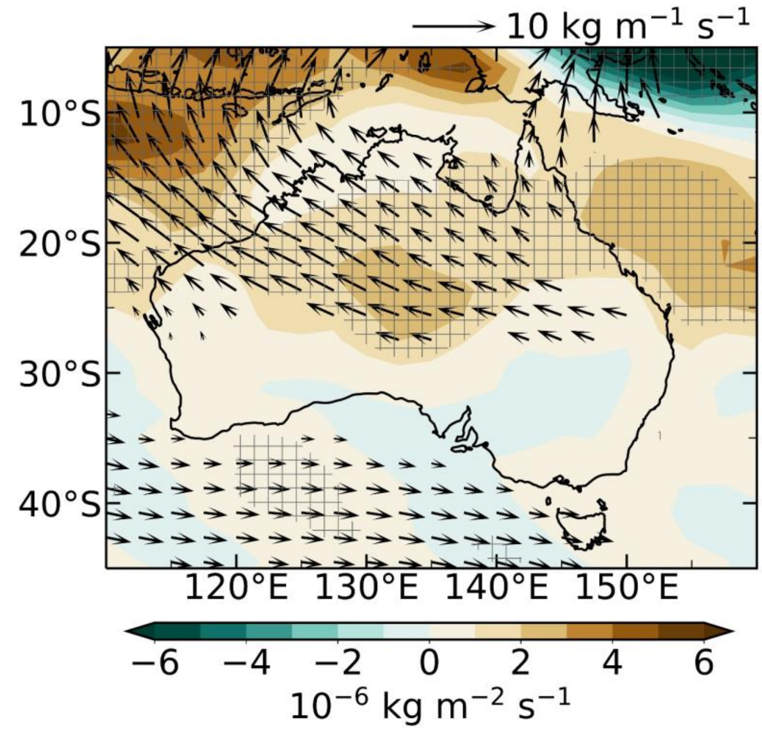

Figure S19. Simulated changes in vertically-integrated moisture flux and its divergence in Australia due to aerosol changes in China between 2013 and 2019. Spatial distributions of simulated differences in annual mean vertically integrated moisture flux (unit: kg m^{-1} s^{-1}, vectors) and its divergence (unit: kg m^{-2} s^{-1}, shades) in Australia between BASE and CHN (CHN minus BASE). Only moisture fluxes which are statistically significant at the 90% confidence level are shown. The shaded areas indicate divergences are statistically significant at the 90% confidence level.

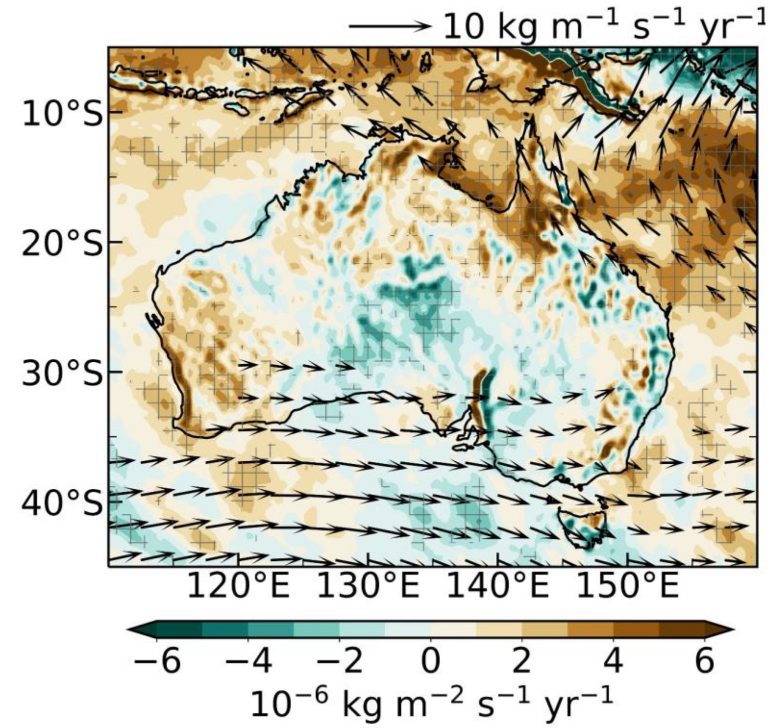

Figure S20. Linear trends in vertically integrated moisture flux and its divergence in Australia during 2010–2019. Linear trends in annual mean vertically integrated moisture flux (unit: kg m^{-1} s^{-1} yr^{-1}, vectors) and its divergence (unit: kg m^{-2} s^{-1} yr^{-1}, shades) in Australia during 2010–2019 from ERA5. Only trends of moisture fluxes which are statistically significant at the 90% confidence level are shown. The shaded areas indicate trends of the divergences are statistically significant at the 90% confidence level.

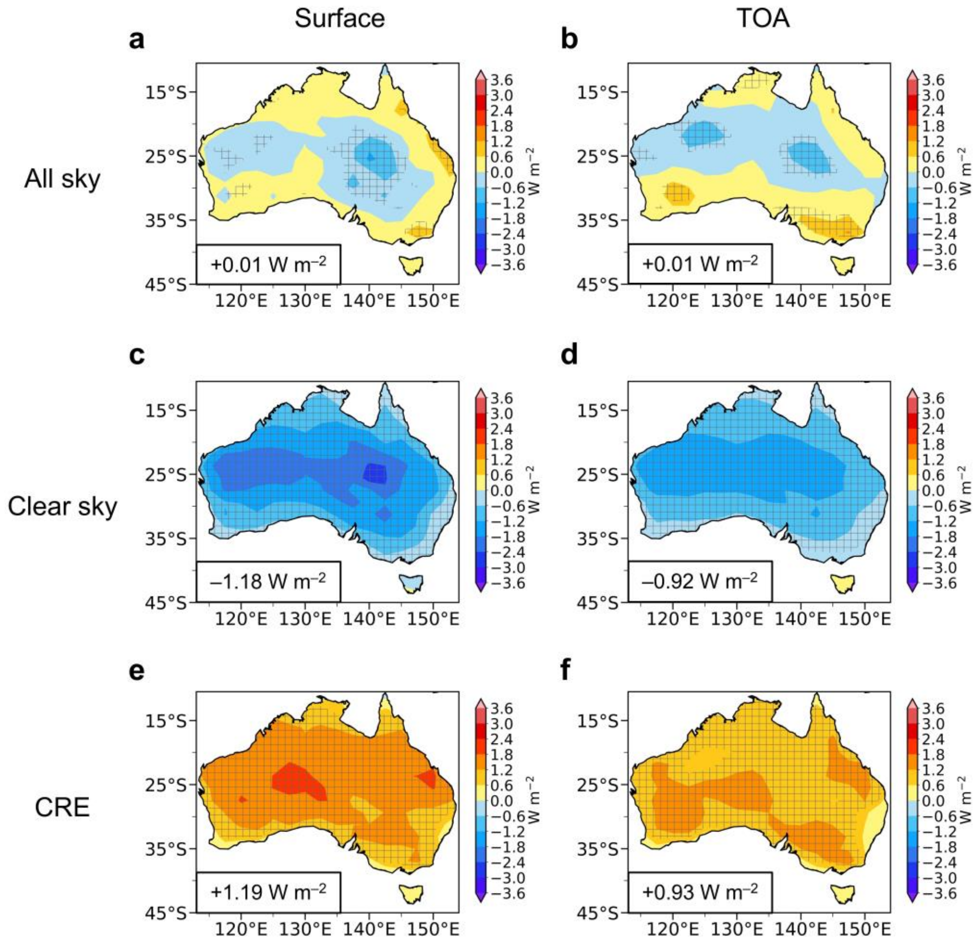

Figure S21. Simulated changes in surface and Top of the Atmosphere (TOA) net total radiative flux under all sky conditions, under clear sky conditions, and from cloud radiative effects in Australia due to aerosol changes in China between 2013 and 2019. Spatial distributions of simulated differences in annual mean surface (**a**, **c**, and **e**) and Top of the Atmosphere (TOA, **b**, **d**, and **f**) net total radiative flux (unit: W m^{-2}) under all sky conditions (**a** and **b**), under clear sky conditions (**c** and **d**), and from cloud radiative effects (CRE, **e** and **f**) in Australia between BASE and CHN (CHN minus BASE). Cloud radiative effects refer to differences under all sky and clear sky conditions (All sky minus Clear sky). The shaded areas indicate results are statistically significant at the 90% confidence level. Regional averages of the responses over Australia are noted at the bottom-left corner of each panel.

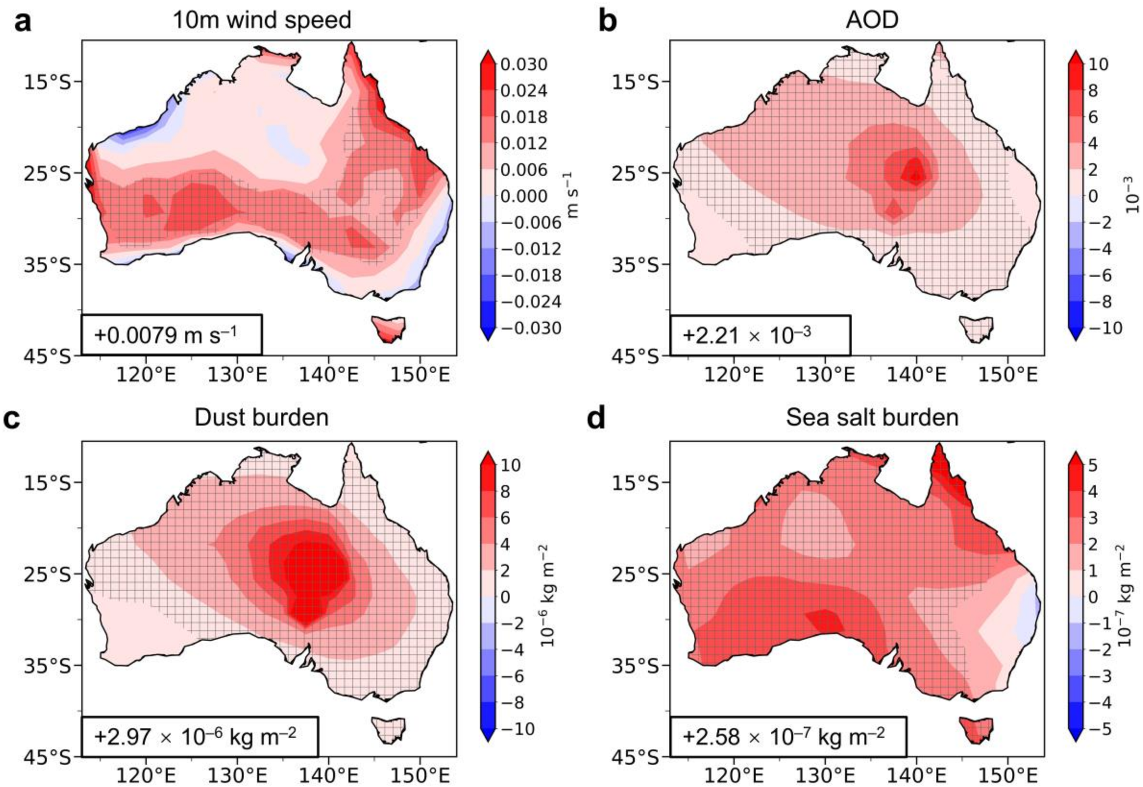

Figure S22. Simulated changes in 10m wind speed, AOD, dust burden, and sea salt burden in Australia due to aerosol changes in China between 2013 and 2019. Spatial distributions of simulated differences in annual mean 10m wind speed (**a**, unit: m s^{-1}), AOD (**b**, unitless), dust burden (**c**, unit: kg m^{-2}), and sea salt burden (**d**, unit: kg m^{-2}) in Australia between BASE and CHN (CHN minus BASE). The shaded areas indicate results are statistically significant at the 90% confidence level. Regional averages of the responses over Australia are noted at the bottom-left corner of each panel.

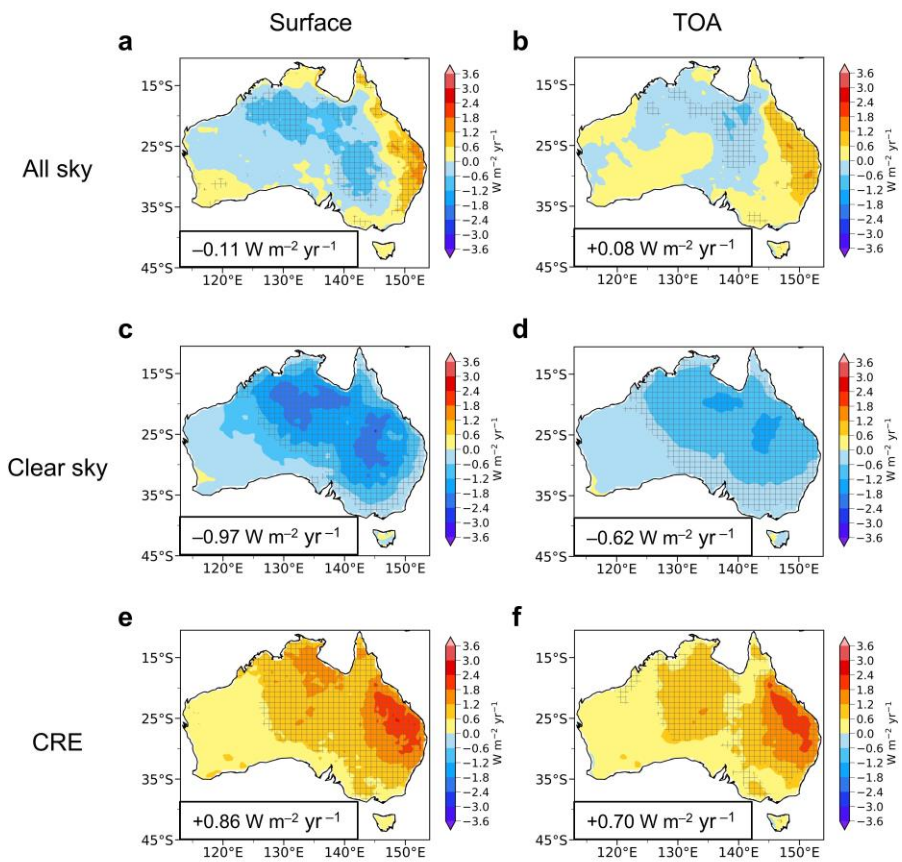

Figure S23. Linear trends of observed surface and Top of the Atmosphere (TOA) net total radiative flux under all sky conditions, under clear sky conditions, and from cloud radiative effects in Australia based on ERA5. Spatial distributions of linear trends of annual mean surface (**a**, **c**, and **e**) and Top of the Atmosphere (TOA, **b**, **d**, and **f**) net total radiative flux (unit: W m^{-2} yr^{-1}) under all sky conditions (**a** and **b**), under clear sky conditions (**c** and **d**), and from cloud radiative effects (CRE, **e** and **f**) in Australia during 2010–2019 from ERA5. Cloud radiative effects refer to differences under all sky and clear sky conditions (All sky minus Clear sky). The shaded areas indicate trends are statistically significant at the 90% confidence level. Regional averages over Australia are noted at the bottom-left corner of panels.

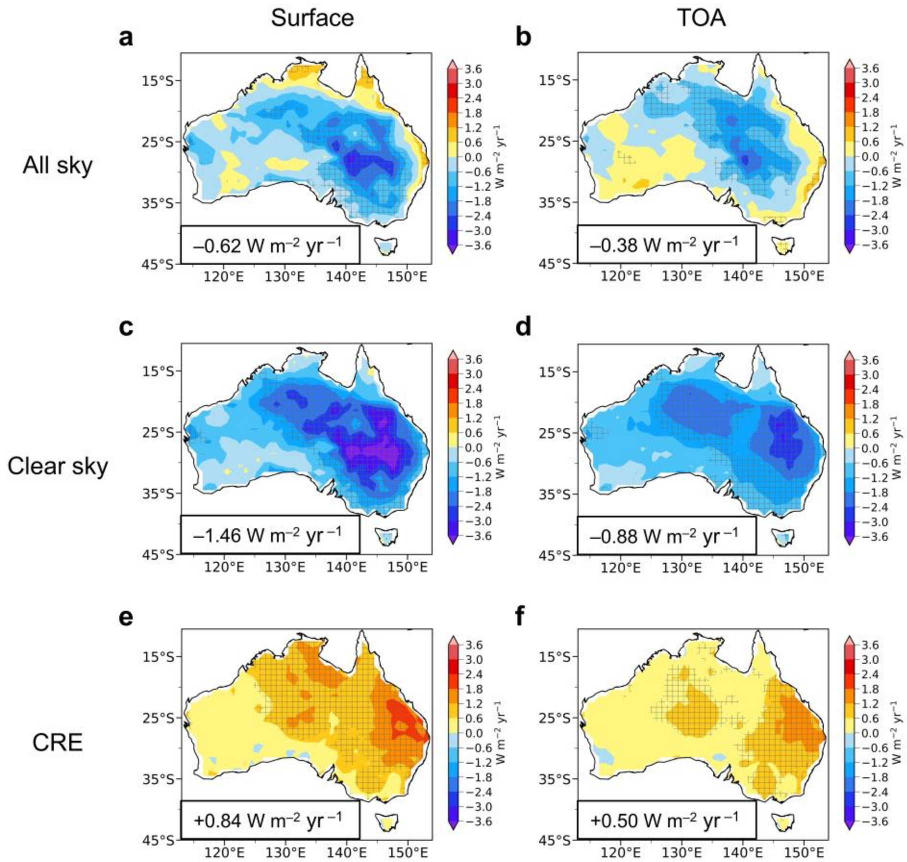

Figure S24. Linear trends of observed surface and Top of the Atmosphere (TOA) net total radiative flux under all sky conditions, under clear sky conditions, and from cloud radiative effects in Australia based on CERES-EBAF. Spatial distributions of linear trends of annual mean surface (**a**, **c**, and **e**) and Top of the Atmosphere (TOA, **b**, **d**, and **f**) net total radiative flux (unit: W m^{-2} yr^{-1}) under all sky conditions (**a** and **b**), under clear sky conditions (**c** and **d**), and from cloud radiative effects (CRE, **e** and **f**) in Australia during 2010–2019 from CERES-EBAF. Cloud radiative effects refer to differences under all sky and clear sky conditions (All sky minus Clear sky). The shaded areas indicate trends are statistically significant at the 90% confidence level. Regional averages over Australia are noted at the bottom-left corner of panels.

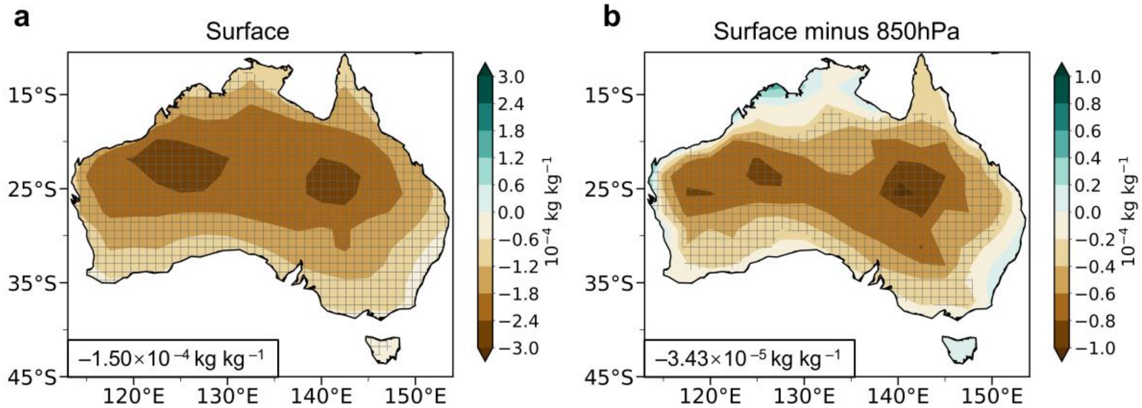

Figure S25. Simulated changes in surface specific humidity and specific humidity differences between surface and 850 hPa in Australia due to aerosol changes in China between 2013 and 2019. Spatial distributions of simulated differences in annual mean surface specific humidity (**a**, unit: kg kg^{-1}) and differences in specific humidity between surface and 850 hPa (**b**, Surface minus 850 hPa, unit: kg kg^{-1}) in Australia between BASE and CHN (CHN minus BASE). The shaded areas indicate results are statistically significant at the 90% confidence level. Regional averages over Australia are noted at the bottom-left corner of each panel.

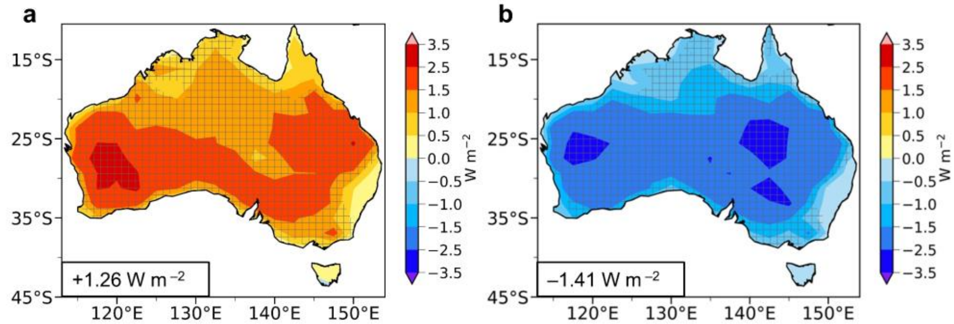

Figure S26. Simulated changes in surface upward sensible and latent heat flux in Australia due to aerosol changes in China between 2013 and 2019. Spatial distributions of simulated differences in annual mean surface upward sensible (**a**) and latent (**b**) heat flux (unit: W m^{-2}) in Australia between BASE and CHN (CHN minus BASE). The shaded areas indicate results are statistically significant at the 90% confidence level. Regional averages over Australia are noted at the bottom-left corner of each panel.

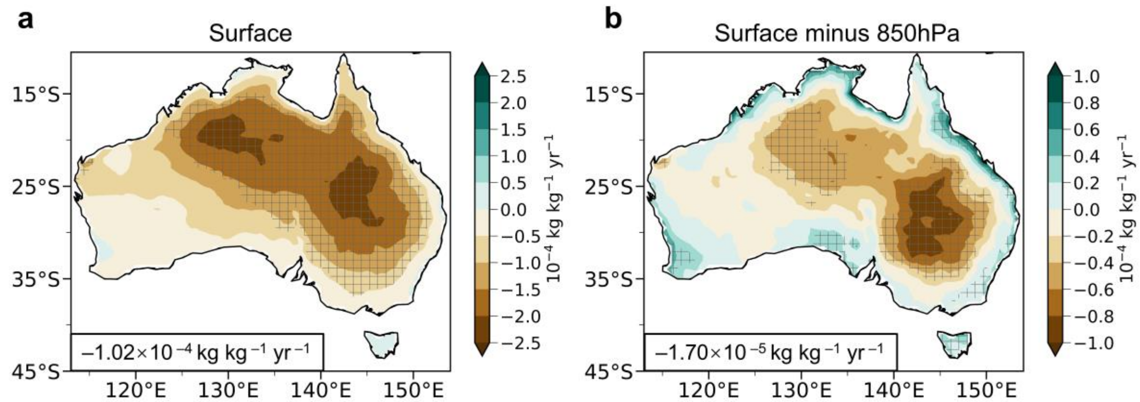

Figure S27. Linear trends of observed surface specific humidity and specific humidity differences between surface and near-surface air in Australia. Spatial distributions of linear trends of annual mean surface specific humidity (**a**, unit: kg kg^{-1} yr^{-1}) and differences in specific humidity between surface and near-surface air (**b**, Surface minus 850 hPa, unit: kg kg^{-1} yr^{-1}) in Australia during 2010–2019 from ERA5. The shaded areas indicate trends are statistically significant at the 90% confidence level. Regional averages over Australia are noted at the bottom-left corner of each panel.

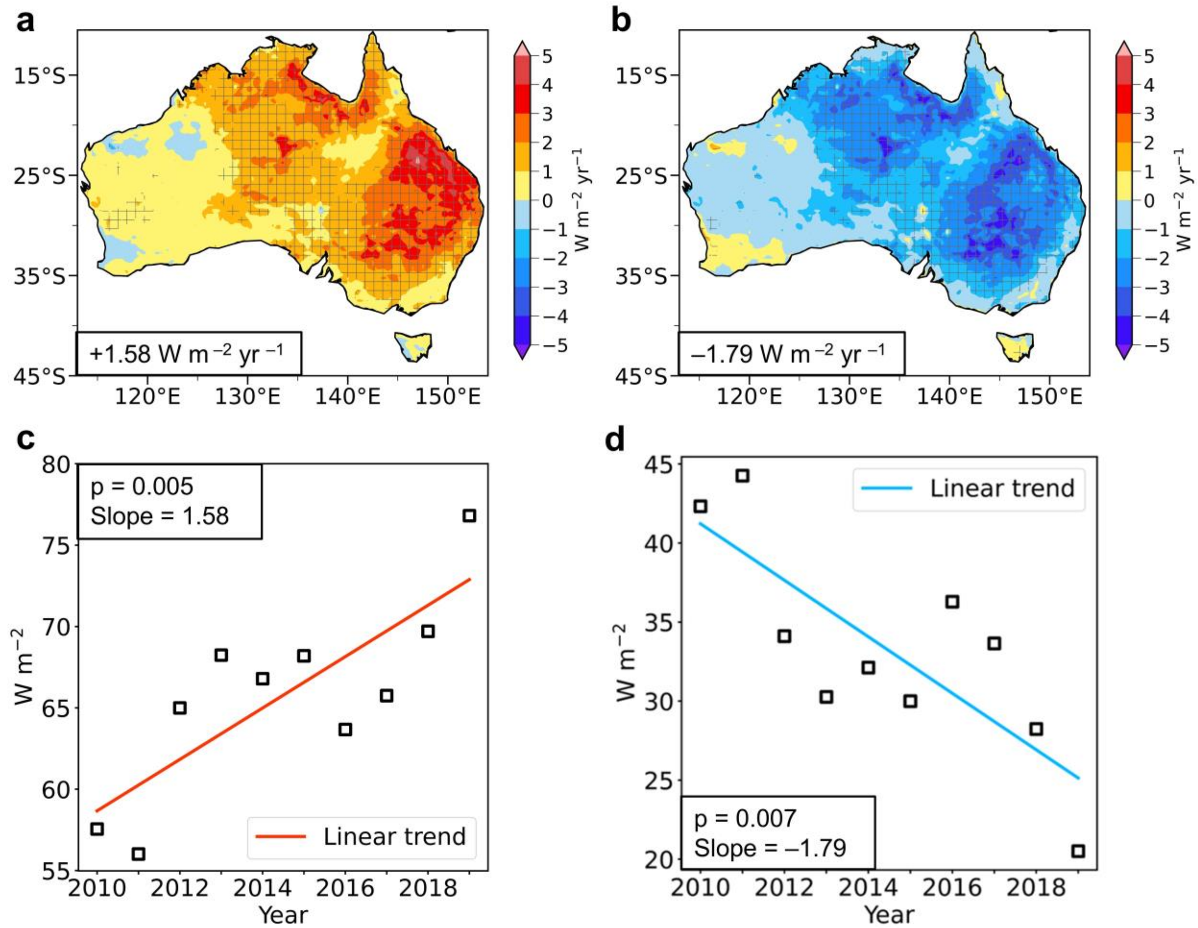

Figure S28. Linear trends of observed surface sensible and latent heat flux in Australia during 2010–2019. Spatial distributions of linear trends (**a** and **b**) and time series (**c** and **d**) of annual mean surface sensible (**a** and **c**) and latent (**b** and **d**) heat flux (unit: W m^{-2} yr^{-1}) in Australia during 2010–2019 from ERA5 reanalysis. The shaded areas indicate trends are statistically significant at the 90% confidence level. Regional averages over Australia are noted at the bottom-left corner of panels a and b. The p values and slopes of these linear trends are noted in panels c and d.

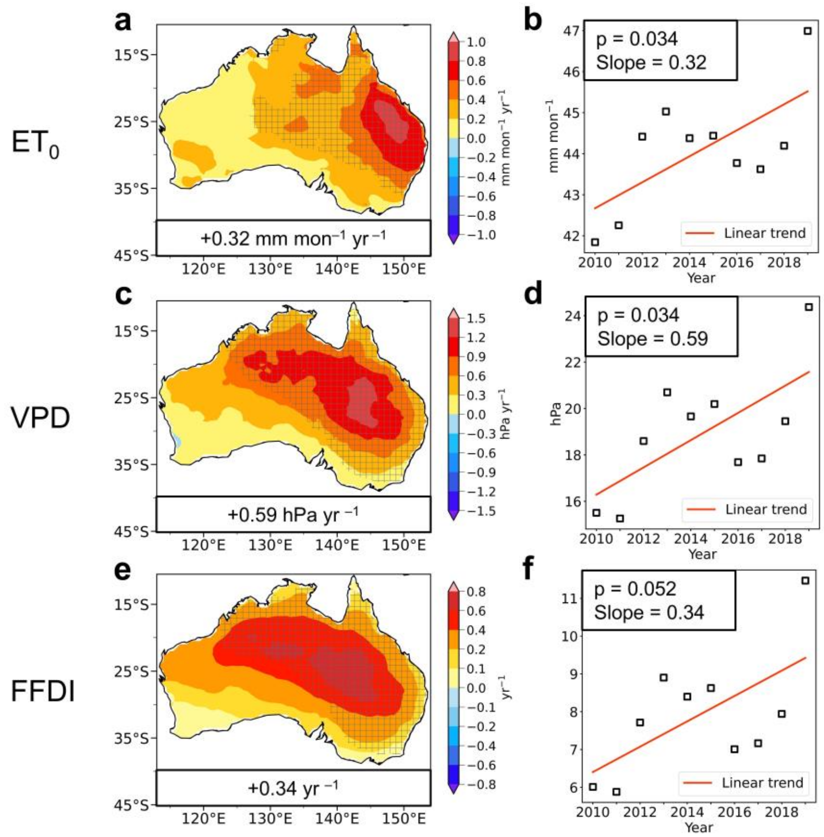

Figure S29. Linear trends of reference potential evapotranspiration, vapor pressure deficit, and McArthur forest fire danger index during fire seasons in Australia. Spatial distributions of linear trends (**a**, **c**, and **e**) and time series (**b**, **d** and **f**) of annual mean reference potential evapotranspiration (ET_0, **a** and **b**), vapor pressure deficit (VPD, **c** and **d**), and McArthur forest fire danger index (FFDI, **e** and **f**) during fire seasons (austral spring and summer, from September to the February of the next year) in Australia during 2010–2019 from ERA5. The shaded areas indicate trends are statistically significant at the 90% confidence level. Regional averages over Australia are noted at the bottom of panels a, c, and e. The p values and slopes of these linear trends are noted in panels b, d, and f.